Nonadiabatic Renormalization of the Phonon Dispersion in Monolayer and Bilayer Graphene

Jiade Li[1,2,*] Jilin Tang,[3,4,*] Zhiyu Tao,[1,5] Ruochen Shi,[2] Xin Gao,[3,4] Siwei Xue[6,1] Xiaoyin Gao,[3] Weiyu Sun,[7,4] Guangyao Miao[1] Zhibin Su,[1,5] Xiongfei Shi[1,5] Shiqi Hu,[1] Ruilin Mao,[2] Xiaowen Zhang,[2] Peiyi He,[2] Weihua Wang,[1] Peng Gao,[2] Hailin Peng,[3,7,4,†] Chao Lian,[1,‡] Jiandong Guo,[1,5,§] and Xuetao Zhu[1,5,∥]

[1]*Beijing National Laboratory for Condensed Matter Physics and Institute of Physics, Chinese Academy of Sciences, Beijing 100190, China*
[2]*International Center for Quantum Materials, and Electron Microscopy Laboratory, School of Physics, Peking University, Beijing 100871, China*
[3]*Center for Nanochemistry, Beijing Science and Engineering Center for Nanocarbons, Beijing National Laboratory for Molecular Sciences, College of Chemistry and Molecular Engineering, Peking University, Beijing 100871, China*
[4]*Beijing Graphene Institute (BGI), Beijing 100095, China*
[5]*School of Physical Sciences, University of Chinese Academy of Sciences, Beijing 100049, China*
[6]*Department of Physics, Fuzhou University, Fuzhou 350108, Fujian, China*
[7]*Academy for Advanced Interdisciplinary Studies, Peking University, Beijing 100871, China*

Nonadiabatic effects profoundly influence lattice dynamics, resulting in phonon renormalizations not only at the center of Brillouin zone (BZ), but also across the entire dispersion at finite momenta. These nonadiabatic phenomena exhibit clear dimensional dependencies and remain largely unexplored experimentally in low-dimensional systems. Here, we utilize high-resolution electron energy loss spectroscopy to investigate nonadiabatic phonon dispersion renormalization in monolayer graphene (MLG) and Bernal bilayer graphene (BLG). We present comprehensive phonon spectra measurements for both MLG and BLG across the full BZ. The high-resolution data reveal an intriguing "W" -shaped dispersion for the longitudinal optical phonon in MLG and a "V" -shaped dispersion in BLG near the BZ center, in contrast to the conventional "U" -shaped parabolic dispersions. Combining theoretical analysis, these anomalous phonon renormalizations are demonstrated to originate from nonadiabatic electron-phonon couplings. The comparative study of MLG and BLG gives a generic understanding of the impact of nonadiabatic effects on phonon dispersions in doped two-dimensional systems.

The Born-Oppenheimer approximation [1], one of the cornerstones of condensed matter physics, assumes that the motion of electrons and ions can be separated by the huge differences in their masses and velocities. This adiabatic approximation facilitates the treatment of solid systems by allowing the electronic wave function to be solved independently of the ionic motions. However, this approximation breaks down when the energy scales of electronic motions (E_F, the Fermi energy) and ionic vibrations ($\hbar\omega$, the phonon energy) become comparable, giving rise to nonadiabatic effects. Nonadiabatic effects are widely believed to influence a range of physical phenomena,

including superconductivity [2–5], transport behaviors [6], and optical properties [7,8].

Among the various consequences of nonadiabatic effects, one of the most notable manifestations is phonon renormalization. Typically, phonon renormalization resulting from electron-phonon couplings (EPCs) is known as the well-established Kohn anomaly [9,10]. Although phonon renormalization is affected by both the amplitude of the electron-phonon scattering probability and the electron response to ionic vibrations [i.e., the Lindhard response function, $\chi(q,\omega)$, where q denotes the momentum transfer and ω represents the phonon frequency], the nonadiabatic effects are believed to mainly modulate the latter [11]. In the adiabatic limit ($\hbar\omega \ll E_F$), electrons can respond instantaneously to ionic motions [Fig. 1(a)], effectively decoupling from the ions. This results in the electron response being well captured by the static Lindhard response function $\chi(q, \omega = 0)$. For an ideal electron gas, although the real part of the static Lindhard function

*These authors contributed equally to this work.
†Contact author: hlpeng@pku.edu.cn
‡Contact author: chaolian@iphy.ac.cn
§Contact author: jdguo@iphy.ac.cn
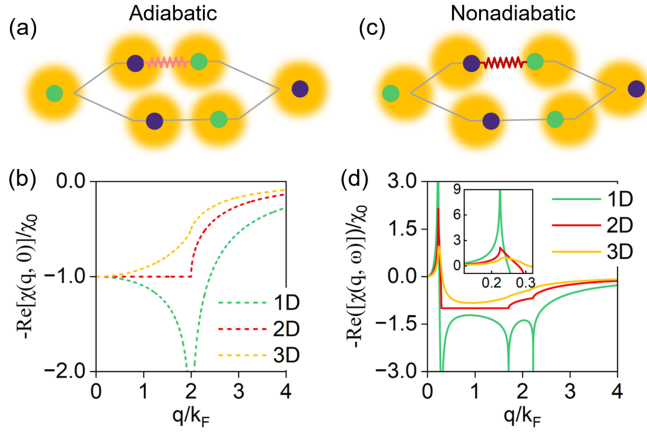∥Contact author: xtzhu@iphy.ac.cn

FIG. 1. Schematic of nonadiabatic effects. (a),(c) Depiction of electron and ion behaviors in adiabatic and nonadiabatic scenarios, respectively. The small circles represent ions, and the large orange background represents electron clouds. In the nonadiabatic condition, the failure of electrons to adjust instantaneously to the vibrational state of ions leads to dynamic electron screening. (b),(d) Static and dynamic Lindhard response functions for 1D (green curves), 2D (red curves), and 3D (orange curves) electron gas systems, respectively. The inset in (d) shows the details of dynamic Lindhard response functions at small momentum. k_F is the Fermi wave vector. The Lindhard functions are renormalized by $\chi_0 = \mathrm{Re}[\chi(q = 0, \omega = 0)]$.

exhibits significant differences across one-, two-, and three-dimensional (1D, 2D, and 3D) systems [Fig. 1(b)], all of them tend to cause phonon softening.

Conversely, under nonadiabatic conditions ($\hbar\omega \sim E_F$), comparable motion velocities of electrons and ions disrupt this instantaneous response [Fig. 1(c)], preventing the prompt screening of ion potentials. Such effects are generally described by the dynamic Lindhard function. In this nonadiabatic regime, the real part of the dynamic Lindhard function exhibits a peak at a small momentum near zero in the 3D case [Fig. 1(d)]. Intriguingly, as the system dimensionality decreases to 2D and 1D, the peak evolves into a pronounced singularity [inset in Fig. 1(d)]. Such a strong electron response suggests a substantial influence on lattice dynamics, leading to dynamic interactions that modify the force constants between ions. Consequently, nonadiabatic effects induce complex phonon renormalization, particularly causing phonon hardening at small momenta—a phenomenon that goes beyond the expectations of the adiabatic approximation.

Previous nonadiabatic effects on phonons have primarily focused on the long-wavelength limit. Theoretical analyses and optical spectroscopic investigations have confirmed the existence of nonadiabatic Kohn anomalies at the center of the Brillouin zone (BZ) in a variety of materials, including monolayer graphene (MLG) [12–14], bilayer graphene (BLG) [15–17], carbon nanotubes [18,19], intercalated graphite [20,21], and transition metals [22], among others. To date, experimental investigations into the impact of

nonadiabatic effects on phonon dispersions beyond the BZ center have been conducted only in the 3D material, diamond [23]. However, no obvious phonon nonanalytic behavior in the phonon dispersions was observed in diamond, as the high dimensionality (3D) weakens the nonadiabatic electron response.

Nonadiabatic renormalizations of phonon dispersions are expected to be more pronounced in low-dimensional systems, as shown in Fig. 1(d), but experimental studies remain scarce due to the challenges in accurately capturing phonon dispersion in these systems. One-dimensional systems are anticipated to exhibit the strongest nonadiabatic effects; however, challenges in sample preparation impede experimental studies. Two-dimensional systems, with their inherent stability, present ideal candidates for such investigations. Nevertheless, even for the most well-studied 2D materials, such as MLG and Bernal (AB-stacked) BLG, the specific effects of nonadiabatic interactions on phonon dispersion are still not well understood. In the case of MLG, theoretical predictions regarding the impact of nonadiabatic effects on phonon dispersions remain inconsistent [24–26]. For BLG, studies on its nonadiabatic phonon dispersions are notably lacking. This gap is particularly significant given the superconductivity in Bernal BLG has been recently observed experimentally [27–29] and is believed to be linked to EPC [30]. Therefore, there is an urgent need to investigate nonadiabatic effects in MLG and BLG through high-resolution measurements of their phonon dispersions.

Here, we employ state-of-the-art high-resolution electron energy loss spectroscopy with 2D imaging detection of energy and momentum [2D high-resolution electron energy loss spectroscopy (2D-HREELS), Fig. 2(a)] [31] to map the full phonon spectra of MLG and BLG. Our measurements unveiled distinct, anomalous, and nonanalytic dispersion behaviors in the longitudinal optical (LO) phonons for both MLG and BLG. Theoretical analysis further attributes these anomalies to nonadiabatic phonon dispersion renormalization, highlighting notable differences and interrelations between the LO modes of MLG and BLG. This analysis of nonadiabatic phonon dynamics enhances our understanding of the physics in MLG and BLG and is crucial for future research on EPCs in low-dimensional materials.

Sample information and experimental setup—The quasifreestanding MLG employed in this study was synthesized on a Cu(111) substrate using chemical vapor deposition. Bernal BLG was fabricated through the exfoliation of a graphene layer from a Cu(111) substrate and subsequent transfer onto the same graphene/Cu(111) sample, ensuring sample continuity. 2D-HREELS experiments were performed at room temperature, using an electron beam energy of 110 eV and an incident angle of 60°. The energy and momentum resolutions are 3.5 meV and 0.035 Å^{-1}, respectively [Fig. S2 in Supplemental Material (SM) [32]]. Additionally, *in situ* angle-resolved photoemission spectroscopy measurements were conducted using the helium
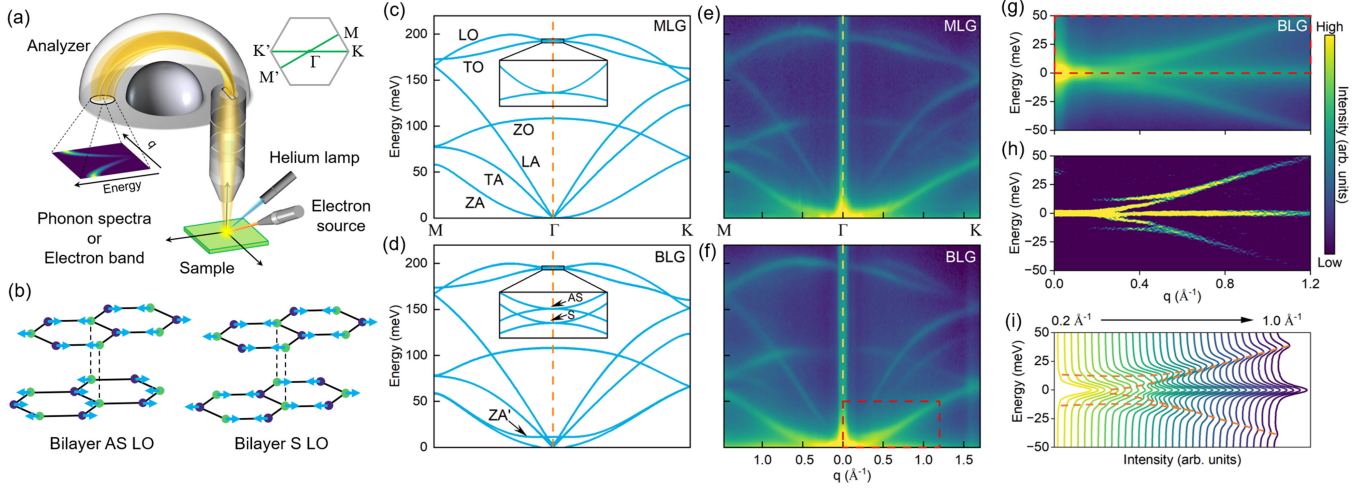
FIG. 2. Phonon spectra of MLG and BLG. (a) A schematic of the experimental setup. Inset: schematic of the BZ. (b) Lattice vibrations of the S LO and AS LO modes in BLG. (c),(d) Calculated phonon dispersions of MLG and BLG along the M-Γ-K paths, respectively. (e),(f) 2D-HREELS mappings of the phonon spectra for MLG and BLG along the M-Γ-K paths, respectively. (g) 2D-HREELS mappings of the ZA' and ZA modes in the energy loss and energy gain regions. The energy loss region corresponds to the area in the red box in (f). (h),(i) The second derivative results and stacked energy distribution curves corresponding to (g), respectively. The orange curves in (i) are guides to the eye.

lamp integrated into the experimental setup [Fig. 2(a)] to assess the doping levels of the samples. Experimental details can be found in SM [32].

Phonon spectra of monolayer and bilayer graphene—
The calculated adiabatic phonon dispersions of MLG and BLG along the M-Γ-K path are depicted in Figs. 2(c) and 2(d), respectively ("Methods" in SM [32]). The transverse, longitudinal, and out-of-plane acoustic and optical (TA, LA, ZA, TO, LO, and ZO) modes of MLG are labeled on the calculated phonon branches. Compared with MLG, BLG exhibits a doubling of phonon branches due to the emergence of interlayer antisymmetric vibrational modes between graphene layers. Despite the weak interlayer coupling, which typically results in minimal energy separation between symmetric and antisymmetric modes, the antisymmetric out-of-plane acoustic mode (ZA') is an exception, showing a significant energy gap that is characteristic of its bilayer structure.

Using 2D-HREELS, we mapped the phonon spectra of MLG and BLG along the M-Γ-K path [Figs. 2(e) and 2(f), respectively]. Remarkably, the measured phonon dispersions show excellent agreement with the calculated results [Figs. 2(c) and 2(d)]. For MLG, the ZA mode does not vanish at the BZ center but instead opens a gap of ~6 meV due to the substrate effect [Fig. S3(a) in the SM [32]]. For BLG, the dispersion of ZA' mode, also exhibiting a clear gap at the BZ center, is accurately captured in our measurement [Figs. 2(g)–2(i)]. The ZA' phonon is called the breathing mode, and the energy gap size characterizes the strength of interlayer coupling. Our measured results show that the ZA' branch exhibits a flat dispersion with an 11 meV energy gap at small momentum [see Fig. S3(b) in

the SM [32] for fitting results], which is in good agreement with previous theoretical reports on Bernal BLG [33].

It is important to note that the spectral intensities of phonons in the 2D-HREELS are determined by the electron scattering selection rules [53]. In the Γ-M direction, the vibrational eigenvectors of TO phonons are odd parity with respect to the scattering plane, resulting in zero scattering intensity and thus no visibility in the HREELS spectra [53–55]. This allows the dispersion of LO phonons to be distinctly identified and analyzed. In BLG, the LO phonons comprise both interlayer symmetric (S) and antisymmetric (AS) vibrations [Fig. 2(b)], with the latter being dipole active and dominating the scattering intensity [17,56]. Generally, the intensity of dipole scattering is much greater than that of impact scattering [53], which is consistent with the ratio of LO phonons intensities in MLG and BLG (Fig. S4 in SM [32]). Therefore, the LO phonons observed in BLG are assigned to the AS mode. As discussed in the following sections, correctly identifying phonon modes is crucial for investigating nonadiabatic EPCs.

Nonadiabatic renormalization of phonon dispersion—
While the experimental and calculated global phonon spectra of MLG and BLG are generally in good agreement, high-resolution measurements reveal that the dispersions of LO phonons display anomalous behaviors near the BZ center, deviating from the results predicted by the adiabatic approximation. Figures 3(a) and 3(b) illustrate the second derivative results of the 2D-HREELS spectra along the M'-Γ-M path [inset in Fig. 2(a)], providing a clearer visualization of phonon dispersion compared to original spectra. In MLG, the LO phonon exhibits a higher energy near the Γ point with an upward convex curvature, forming
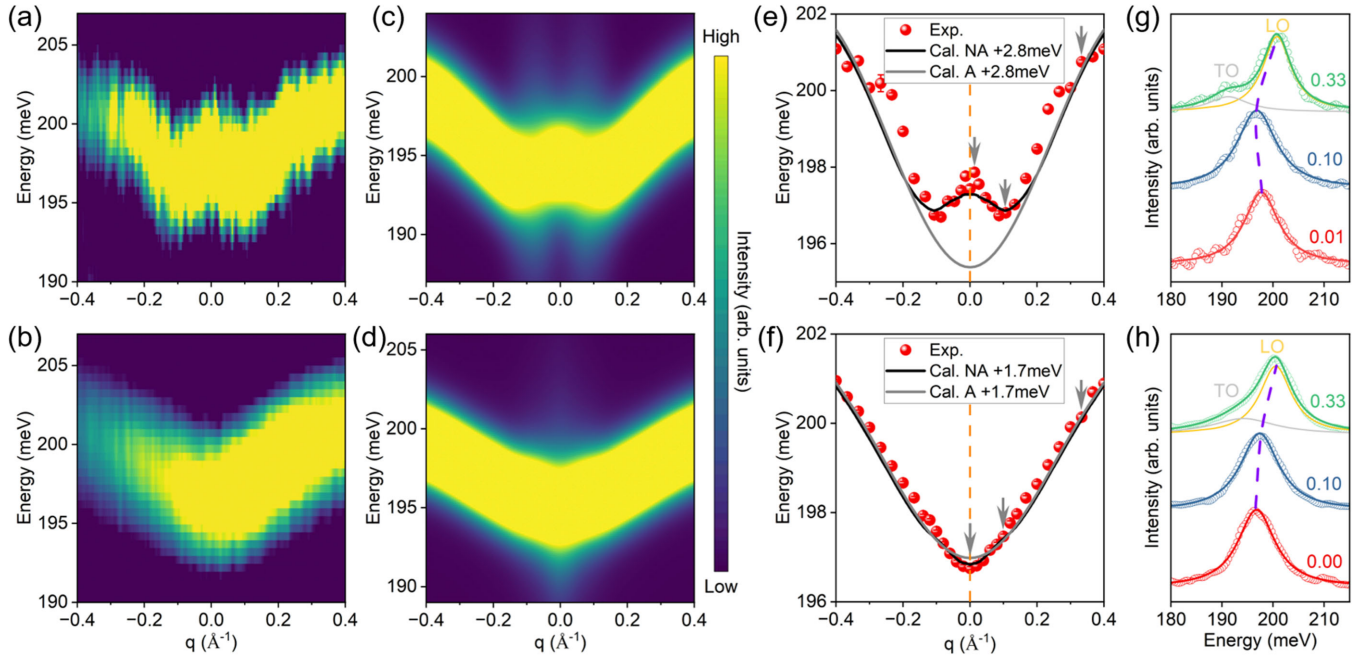
FIG. 3. Nonadiabatic phonon dispersions of MLG and BLG. (a) The second derivative spectra of the LO mode of MLG along M′-Γ-M path. (c) Calculated nonadiabatic phonon spectral functions for the LO mode of MLG. (e) LO phonon dispersion data of MLG. The data are the fitting results of the energy distribution curves extracted from the original 2D-HREELS spectrum. The gray (black) curve represents the results from (non)adiabatic calculations. (g) Typical fitting results (solid lines) for energy distribution curves (open circles) at momenta of 0.01 Å⁻¹ (red), 0.10 Å⁻¹ (blue), and 0.33 Å⁻¹ (green) of MLG [corresponding to the gray arrows in (e)]. The purple dashed line is the guide line for the peak position. (b),(d),(f),(h) Results for the AS LO phonon of BLG corresponding to (a),(c),(e),(g), respectively. The calculated curves in (e) and (f) are shifted by 2.8 and 1.7 meV, respectively.

a "W"-shaped dispersion as momentum (absolute value) increases [Fig. 3(a)]. Conversely, for BLG, the energy of AS LO phonon is minimized at the Γ point, with energy rising as momentum increases to form a "V"-shaped dispersion [Fig. 3(b)]. These observed dispersions align closely with our fitted data [Figs. 3(e)–3(h) for MLG and BLG, respectively]. The "W" and "V"-shaped dispersions around the BZ center exhibit clear nonanalytic behaviors, distinct from the adiabatic "U"-shaped parabolic dispersions [inset in Figs. 2(c) and 2(d)], demonstrating anomalous renormalization of the LO phonons beyond the adiabatic approximation.

To comprehensively understand and assess the overall nonadiabatic dispersion behaviors, we calculated the nonadiabatic spectral functions of the EPC for the LO modes of MLG and BLG. The nonadiabatic spectral function is given by [11]

$$A(\boldsymbol{q}, \omega) = \frac{1}{\pi} \operatorname{Im} \left[\frac{2\omega_0(\boldsymbol{q})}{\omega^2 - \omega_0^2(\boldsymbol{q}) - 2\omega_0(\boldsymbol{q})\Pi^{\mathrm{NA}}(\boldsymbol{q}, \omega)} \right], \quad (1)$$

where $\omega_0(\boldsymbol{q})$ is the adiabatic phonon frequency at momentum $\boldsymbol{q}$ [as presented in Figs. 2(c) and 2(d)], calculated using the density-functional perturbation theory ("Methods"). $\Pi^{\mathrm{NA}}(\boldsymbol{q}, \omega)$ is the nonadiabatic phonon self-energy, defined as

$$\hbar\Pi^{\mathrm{NA}}(\boldsymbol{q}, \omega) = 2\sum_{mn} \int \frac{d\boldsymbol{k}}{\Omega_{\mathrm{BZ}}} |g_{mn}(\boldsymbol{k}, \boldsymbol{q})|^2$$
$$\times \left[\frac{f_{n,\boldsymbol{k}} - f_{m,\boldsymbol{k}+\boldsymbol{q}}}{\varepsilon_{m,\boldsymbol{k}+\boldsymbol{q}} - \varepsilon_{n,\boldsymbol{k}} - \hbar(\omega + i\delta)} \right.$$
$$\left. - \frac{f_{n,\boldsymbol{k}} - f_{m,\boldsymbol{k}+\boldsymbol{q}}}{\varepsilon_{m,\boldsymbol{k}+\boldsymbol{q}} - \varepsilon_{n,\boldsymbol{k}}} \right], \quad (2)$$

where $\varepsilon_{n(m),\boldsymbol{k}}$ and $f_{n(m),\boldsymbol{k}}$ are the electronic band energy and Fermi-Dirac distribution of band index n (m) and momentum $\boldsymbol{k}$, respectively. δ is a positive real infinitesimal and Ω_{BZ} is the volume of BZ. $g_{mn}(\boldsymbol{k}, \boldsymbol{q}) = [\hbar/2M_C\omega_0(\boldsymbol{q})]^{1/2}$ $\langle\psi_{m,\boldsymbol{k}+\boldsymbol{q}}|\partial_{\boldsymbol{q}} v^{\mathrm{KS}}|\psi_{n,\boldsymbol{k}}\rangle$ is the electron-phonon matrix elements. Here, M_C is the mass of carbon atom, $\psi_{n,\boldsymbol{k}}$ is the electron wave function of band n at momentum $\boldsymbol{k}$, and v^{KS} is the lattice-periodic Kohn-Sham potential. The Fermi levels used in calculations are measured *in situ* by angle-resolved photoemission spectroscopy (Fig. S5 in SM [32]). The second term in brackets on the right side of Eq. (2) represents the adiabatic contribution, which is already accounted for in the density-functional perturbation theory calculations ("Methods" in SM [32]). The first term contains the overall (both nonadiabatic and adiabatic) response by including the nonzero phonon frequency ω in the denominator. Therefore, the difference between the two terms represents only the

contribution of the nonadiabatic phonon self-energy. The renormalization of the phonon frequency and lifetime are determined by the real and imaginary parts of the self-energy and are given by the intensity peak and broadening of the spectral functions, respectively.

The introduction of finite ω in Eq. (2) leads to a nonzero nonadiabatic phonon self-energy $\Pi^{\mathrm{NA}}(\boldsymbol{q}, \omega)$, which in turn renormalizes the adiabatic phonon frequency via Eq. (1). As shown in Figs. 3(c) and 3(d), the nonadiabatic spectral functions from our calculations (convolved with the experimental broadening, for the original results see Fig. S7 in SM [32]) exhibit high consistency with the experimental spectra [Figs. 3(a) and 3(b)], successfully reproducing the distinctive "W"-shaped and "V"-shaped dispersions observed in MLG and BLG, respectively. Figures 3(e) and 3(f) display the comparisons between the fitted experimental data and the calculated nonadiabatic (black) and adiabatic (gray) phonon dispersion curves for the LO phonon in MLG and the AS LO phonon in BLG, respectively. The nonadiabatic calculation results show excellent agreement with the experimental data, whereas the adiabatic calculation results (with "U"-shaped dispersions) significantly deviate from the experimental dispersion.

Doping-dependent nonadiabatic phonon renormalization—The doping behavior of the materials provides crucial insights into the relationship between EPCs and nonadiabatic phonon dynamics. Figures 4(a) and 4(b) present the calculated momentum-resolved EPC strength λ_q for LO phonons in MLG and AS LO phonons in BLG at different Fermi levels ("Methods"). For the LO phonon in MLG, increasing doping levels significantly broaden the momentum range of the electron-phonon interaction. In contrast, the doping effect on the AS LO phonon in BLG is relatively modest. Figures 4(c) and 4(d) show the calculated total (momentum-integrated) EPC strength λ and the nonadiabatic phonon renormalization energy ΔE [57] for LO and AS LO phonons as a function of the Fermi level. For LO phonons, there is a marked concurrent increase in both the λ and the ΔE as doping levels rise. On the other hand, for AS LO phonons, doping does not induce significant changes in either the λ or ΔE. These results demonstrate that the EPC strength and the degree of nonadiabatic phonon renormalization are directly related, suggesting that the nonadiabatic effect should not be ignored in any EPC-related phenomena.

Physical origin of the nonadiabatic phonon renormalization—The distinct roles of nonadiabatic effects on phonon renormalization in MLG and BLG are discussed in detail in the End Matter. Briefly, our analysis reveals that the nonadiabatic phonon renormalization primarily arises from singularity in the dynamic Lindhard function, while the electron-phonon matrix elements modulate the extent of the renormalization. The hardening of LO phonons in MLG is caused by intraband transitions, while the softening of AS LO phonons in BLG is primarily driven by interband
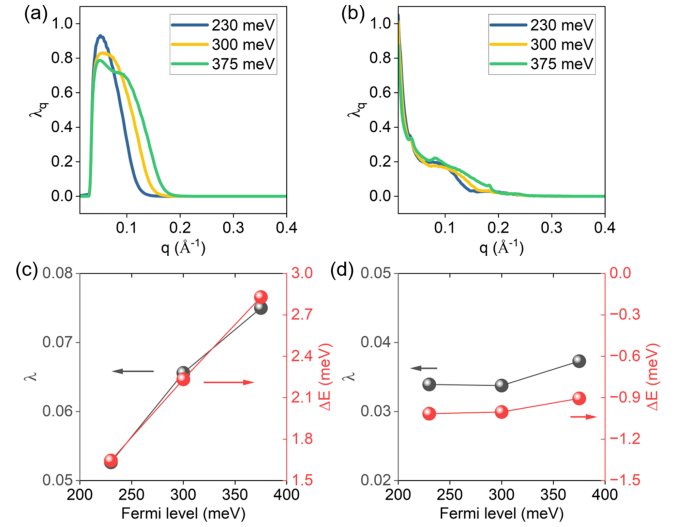

FIG. 4. Doping-dependent EPC and phonon renormalization. (a) Momentum-resolved EPC strength λ_q for the LO phonon in MLG at different Fermi levels. (c) The dependence of the total EPC strength λ and the phonon renormalization energy ΔE of the LO phonon on the Fermi level in MLG. (b),(d) Results for the AS LO phonon of BLG corresponding to (a) and (c), respectively.

transitions. The differences in nonadiabatic renormalizations between LO phonons in MLG and AS LO phonons in BLG are attributed to the symmetry-related EPC mechanisms (further elaborated in the End Matter).

More directly, the nonadiabatic and adiabatic pictures can be more simply analyzed through the denominator of the dynamic Lindhard function

$$\chi^{\mathrm{D}}_{mn}(\boldsymbol{q}, \omega) = \int \frac{d\boldsymbol{k}}{\Omega_{\mathrm{BZ}}} \frac{f_{n,\boldsymbol{k}} - f_{m,\boldsymbol{k}+\boldsymbol{q}}}{\varepsilon_{m,\boldsymbol{k}+\boldsymbol{q}} - \varepsilon_{n,\boldsymbol{k}} - \hbar(\omega + i\delta)}. \quad (3)$$

In the nonadiabatic case, phonons possess a finite energy of $\hbar\omega$. For intraband transitions, the energy difference between the initial and final electronic states is $\Delta\varepsilon = \varepsilon_{\boldsymbol{k}+\boldsymbol{q}} - \varepsilon_{\boldsymbol{k}} \approx v_F q$, where v_F is the Fermi velocity. Therefore, when $q < \hbar\omega/v_F$, we have $\Delta\varepsilon < \hbar\omega$, and the electron-hole dissipation channel for the phonons is blocked. In contrast, in the adiabatic case, since the phonon energy is assumed to be zero, the electron-hole dissipation channel remains open. As a result, the LO phonons in MLG harden at small momentum in the nonadiabatic case. For interband transitions of BLG, the energy difference $\Delta\varepsilon$ between the π_1 and π_2 bands is ~400 meV, which is greater than the phonon energy $\hbar\omega$, meaning the electron-hole dissipation channel remains open even at small momentum. In the nonadiabatic case, the finite phonon energy $\hbar\omega$ reduces the difference with $\Delta\varepsilon$, thus causing an increase in dissipation. As a result, the AS LO phonons in BLG soften at small momentum.

Notably, while the nonadiabatic renormalization of the LO phonon in MLG significantly differs from that of the

AS LO phonon in BLG, our calculations and analysis demonstrate that it exhibits similar behavior to the S LO phonon in BLG (Fig. S8 in SM [32] and End Matter). This is reasonable and expected given that the LO phonons of MLG and the S LO phonons of BLG exhibit the same vibrational symmetry. This similarity between the LO phonons in MLG and S LO phonons in BLG, alongside their differences from the AS LO phonons in BLG, aligns with previous studies conducted at the BZ center [13,15–17]. Our results not only reproduce the nonadiabatic phonon renormalization at the BZ center but also demonstrate that this intriguing effect persists at finite momentum.

Discussions—The singularity in the 2D dynamic Lindhard function arises predominantly from dimensional effects rather than the specific characteristics of the electronic bands. This is particularly prominent in our study. Although MLG and BLG feature Dirac linear and parabolic electronic bands, respectively, the LO and S LO phonons exhibit analogous nonadiabatic renormalization behaviors. This suggests that the phonon hardening caused by nonadiabatic effects is generally prominent in doped 2D systems, as predicted in doped monolayer MoS_2, [58] graphane [59], and arsenene [59], among others. This is consistent with the general behavior of the 2D dynamic Lindhard function shown in Fig. 1(d).

Although the extent of phonon dispersion renormalization induced by nonadiabatic effects seems modest, its implications for the fundamental properties of materials, such as superconductivity, are significant. Theoretical studies indicate that nonadiabatic effects can substantially enhance EPC strength, thereby increasing the superconducting transition temperature [60,61]. Given that phonons are believed to mediate the superconductivity in Bernal BLG [30] and magic-angle twisted BLG [62–64], the nonadiabatic nature of the EPC should be considered to properly evaluate their superconducting properties. Additionally, the high-resolution mapping of phonon spectra in BLG using the 2D-HREELS approach offers a promising avenue for further exploration of phonon dispersions and their related physics in magic-angle twisted BLG [65–67] and other twisted systems [68–70].

Data availability—The data that support the findings of this article are openly available [71].

[1] M. Born and R. Oppenheimer, Ann. Phys. (Berlin) **389**, 457 (1927).

[2] C. Grimaldi, L. Pietronero, and S. Strässler, Phys. Rev. Lett. **75**, 1158 (1995).

[3] E. Cappelluti, S. Ciuchi, C. Grimaldi, L. Pietronero, and S. Strässler, Phys. Rev. Lett. **88**, 117003 (2002).

[4] S. Zhang, T. Wei, J. Guan, Q. Zhu, W. Qin, W. Wang, J. Zhang, E. W. Plummer, X. Zhu, Z. Zhang, and J. Guo, Phys. Rev. Lett. **122**, 066802 (2019).

[5] L. Pietronero and S. Strässler, Europhys. Lett. **18**, 627 (1992).

[6] Y. Huang, J. Zhou, G. Wang, and Z. Sun, J. Am. Chem. Soc. **141**, 8503 (2019).

[7] S.-Q. Hu, H. Zhao, X.-B. Liu, Q. Chen, D.-Q. Chen, X.-Y. Zhang, and S. Meng, Phys. Rev. Lett. **133**, 156901 (2024).

[8] J.-M. Lihm and C.-H. Park, Phys. Rev. Lett. **133**, 116402 (2024).

[9] W. Kohn, Phys. Rev. Lett. **2**, 393 (1959).

[10] E. J. Woll and W. Kohn, Phys. Rev. **126**, 1693 (1962).

[11] F. Giustino, Rev. Mod. Phys. **89**, 015003 (2017).

[12] M. Lazzeri and F. Mauri, Phys. Rev. Lett. **97**, 266407 (2006).

[13] S. Pisana, M. Lazzeri, C. Casiraghi, K. S. Novoselov, A. K. Geim, A. C. Ferrari, and F. Mauri, Nat. Mater. **6**, 198 (2007).

[14] A. Das, S. Pisana, B. Chakraborty, S. Piscanec, S. K. Saha, U. V. Waghmare, K. S. Novoselov, H. R. Krishnamurthy, A. K. Geim, A. C. Ferrari, and A. K. Sood, Nat. Nanotechnol. **3**, 210 (2008).

[15] J. Yan, E. A. Henriksen, P. Kim, and A. Pinczuk, Phys. Rev. Lett. **101**, 136804 (2008).

[16] L. M. Malard, D. C. Elias, E. S. Alves, and M. A. Pimenta, Phys. Rev. Lett. **101**, 257401 (2008).

[17] A. B. Kuzmenko, L. Benfatto, E. Cappelluti, I. Crassee, D. van der Marel, P. Blake, K. S. Novoselov, and A. K. Geim, Phys. Rev. Lett. **103**, 116804 (2009).

[18] N. Caudal, A. M. Saitta, M. Lazzeri, and F. Mauri, Phys. Rev. B **75**, 115423 (2007).

[19] V. N. Popov and P. Lambin, Nano Res. **3**, 822 (2010).

[20] A. M. Saitta, M. Lazzeri, M. Calandra, and F. Mauri, Phys. Rev. Lett. **100**, 226401 (2008).

[21] M. P. M. Dean, C. A. Howard, S. S. Saxena, and M. Ellerby, Phys. Rev. B **81**, 045405 (2010).

[22] Y. S. Ponosov and S. V. Streltsov, Phys. Rev. B **94**, 214302 (2016).

[23] F. Caruso, M. Hoesch, P. Achatz, J. Serrano, M. Krisch, E. Bustarret, and F. Giustino, Phys. Rev. Lett. **119**, 017001 (2017).

[24] W.-K. Tse, B. Y.-K. Hu, and S. Das Sarma, Phys. Rev. Lett. **101**, 066401 (2008).

[25] V. N. Popov and P. Lambin, Phys. Rev. B **82**, 045406 (2010).

[26] N. Girotto and D. Novko, J. Phys. Chem. Lett. **14**, 8709 (2023).

[27] H. Zhou, L. Holleis, Y. Saito, L. Cohen, W. Huynh, C. L. Patterson, F. Yang, T. Taniguchi, K. Watanabe, and A. F. Young, Science **375**, 774 (2022).

[28] Y. Zhang, R. Polski, A. Thomson, É. Lantagne-Hurtubise, C. Lewandowski, H. Zhou, K. Watanabe, T. Taniguchi, J. Alicea, and S. Nadj-Perge, Nature (London) **613**, 268 (2023).

[29] C. Li, F. Xu, B. Li, J. Li, G. Li, K. Watanabe, T. Taniguchi, B. Tong, J. Shen, L. Lu, J. Jia, F. Wu, X. Liu, and T. Li, Nature (London) **631**, 300 (2024).

[30] Y.-Z. Chou, F. Wu, J. D. Sau, and S. Das Sarma, Phys. Rev. B **105**, L100503 (2022).

[31] X. Zhu, Y. Cao, S. Zhang, X. Jia, Q. Guo, F. Yang, L. Zhu, J. Zhang, E. W. Plummer, and J. Guo, Rev. Sci. Instrum. **86**, 083902 (2015).

[32] See Supplemental Material at http://link.aps.org/supplemental/10.1103/4x9y-txyy for details about the sample preparation, experimental and theoretical methods, and the influence of transfer process and substrate effects, which includes Figs. S1–S8 and Refs. [11,16,17,31,33–52].

[33] A. I. Cocemasov, D. L. Nika, and A. A. Balandin, Phys. Rev. B **88**, 035428 (2013).

[34] X. Gao, L. Zheng, F. Luo, J. Qian, J. Wang, M. Yan, W. Wang, Q. Wu, J. Tang, Y. Cao, C. Tan, J. Tang, M. Zhu, Y. Wang, Y. Li, L. Sun, G. Gao, J. Yin, L. Lin, Z. Liu, S. Qin, and H. Peng, Nat. Commun. **13**, 5410 (2022).

[35] P. Giannozzi et al., J. Phys. Condens. Matter **21**, 395502 (2009).

[36] P. Giannozzi et al., J. Phys. Condens. Matter **29**, 465901 (2017).

[37] G. Pizzi et al., J. Phys. Condens. Matter **32**, 165902 (2020).

[38] S. Poncé, E. R. Margine, C. Verdi, and F. Giustino, Comput. Phys. Commun. **209**, 116 (2016).

[39] H. Lee, S. Poncé, K. Bushick, S. Hajinazar, J. Lafuente-Bartolome, J. Leveillee, C. Lian, J.-M. Lihm, F. Macheda, H. Mori, H. Paudyal, W. H. Sio, S. Tiwari, M. Zacharias, X. Zhang, N. Bonini, E. Kioupakis, E. R. Margine, and F. Giustino, npj Comput. Mater. **9**, 156 (2023).

[40] J. P. Perdew, K. Burke, and M. Ernzerhof, Phys. Rev. Lett. **77**, 3865 (1996).

[41] D. R. Hamann, Phys. Rev. B **88**, 085117 (2013).

[42] M. J. van Setten, M. Giantomassi, E. Bousquet, M. J. Verstraete, D. R. Hamann, X. Gonze, and G. M. Rignanese, Comput. Phys. Commun. **226**, 39 (2018).

[43] H. J. Monkhorst and J. D. Pack, Phys. Rev. B **13**, 5188 (1976).

[44] S. Baroni, S. de Gironcoli, A. Dal Corso, and P. Giannozzi, Rev. Mod. Phys. **73**, 515 (2001).

[45] F. Giustino, M. L. Cohen, and S. G. Louie, Phys. Rev. B **76**, 165108 (2007).

[46] L. M. Malard, J. Nilsson, D. C. Elias, J. C. Brant, F. Plentz, E. S. Alves, A. H. Castro Neto, and M. A. Pimenta, Phys. Rev. B **76**, 201401(R) (2007).

[47] P. Poncharal, A. Ayari, T. Michel, and J.-L. Sauvajol, Phys. Rev. B **78**, 113407 (2008).

[48] F. Joucken, E. A. Quezada-López, J. Avila, C. Chen, J. L. Davenport, H. Chen, K. Watanabe, T. Taniguchi, M. C. Asensio, and J. Velasco, Phys. Rev. B **99**, 161406(R) (2019).

[49] A. Al Taleb and D. Farías, J. Phys. Condens. Matter **28**, 103005 (2016).

[50] A. Allard and L. Wirtz, Nano Lett. **10**, 4335 (2010).

[51] C. T. Nai, H. Xu, S. J. R. Tan, and K. P. Loh, ACS Nano **10**, 1681 (2016).

[52] A. Al Taleb, H. K. Yu, G. Anemone, D. Farías, and A. M. Wodtke, Carbon **95**, 731 (2015).

[53] H. Ibach and D. L. Mills, Electron Energy Loss Spectroscopy and Surface Vibrations (Academic Press, New York, 2013).

[54] F. de Juan, A. Politano, G. Chiarello, and H. A. Fertig, Carbon **85**, 225 (2015).

[55] C. H. Li, S. Y. Tong, and D. L. Mills, Phys. Rev. B **21**, 3057 (1980).

[56] R. J. Koch, S. Fryska, M. Ostler, M. Endlich, F. Speck, T. Hänsel, J. A. Schaefer, and Th. Seyller, Phys. Rev. Lett. **116**, 106802 (2016).

[57] ΔE, representing the maximum phonon hardening energy at small momentum, is defined as the real part of nonadiabatic phonon self-energy at $q = \hbar\omega/v_F$, where v_F is the Fermi velocity.

[58] P. Garcia-Goiricelaya, J. Lafuente-Bartolome, I. G. Gurtubay, and A. Eiguren, Phys. Rev. B **101**, 054304 (2020).

[59] N. Girotto and D. Novko, Phys. Rev. B **107**, 064310 (2023).

[60] S.-Q. Hu, X.-B. Liu, D.-Q. Chen, C. Lian, E.-G. Wang, and S. Meng, Phys. Rev. B **105**, 224311 (2022).

[61] J. Krsnik, D. Novko, and O. S. Barišić, Phys. Rev. B **110**, L180505 (2024).

[62] F. Wu, A. H. MacDonald, and I. Martin, Phys. Rev. Lett. **121**, 257001 (2018).

[63] B. Lian, Z. Wang, and B. A. Bernevig, Phys. Rev. Lett. **122**, 257002 (2019).

[64] F. Wu, E. Hwang, and S. Das Sarma, Phys. Rev. B **99**, 165112 (2019).

[65] Y. W. Choi and H. J. Choi, Phys. Rev. B **98**, 241412(R) (2018).

[66] X. Liu, R. Peng, Z. Sun, and J. Liu, Nano Lett. **22**, 7791 (2022).

[67] Y. Liu, T. Holder, and B. Yan, The Innovation **2**, 100085 (2021).

[68] Z. Zhang, Y. Wang, K. Watanabe, T. Taniguchi, K. Ueno, E. Tutuc, and B. J. LeRoy, Nat. Phys. **16**, 1093 (2020).

[69] B. Liu, Y.-T. Zhang, R. Qiao, R. Shi, Y. Li, Q. Guo, J. Li, X. Li, L. Wang, J. Qi, S. Du, X. Ren, K. Liu, P. Gao, and Y.-Y. Zhang, Phys. Rev. Lett. **131**, 016201 (2023).

[70] G. Sánchez-Santolino, V. Rouco, S. Puebla, H. Aramberri, V. Zamora, M. Cabero, F. A. Cuellar, C. Munuera, F. Mompean, M. Garcia-Hernandez, A. Castellanos-Gomez, J. Íñiguez, C. Leon, and J. Santamaria, Nature (London) **626**, 529 (2024).

[71] J. Li et al., (2025), 10.6084/m9.figshare.29412191.

End Matter

Band-resolved analysis of nonadiabatic phonon renormalization—To unveil the distinct roles of the nonadiabatic phonon renormalization of LO mode in MLG and AS LO mode in BLG, we delve into the band-resolved electron-phonon matrix elements $g_{mn}(\mathbf{k}, \mathbf{q})$ and the Lindhard term, which signify the probability for the electron-phonon scattering process and the response of electron to lattice vibrations, respectively. The band-resolved nonadiabatic Lindhard function $\chi_{mn}^{\mathrm{NA}}(\mathbf{q}, \omega)$ is defined as the difference between the dynamic $\chi_{mn}^{\mathrm{D}}(\mathbf{q}, \omega)$ and the static (adiabatic) Lindhard $\chi_{mn}(\mathbf{q})$ term

$$\chi_{mn}^{\mathrm{NA}}(\mathbf{q}, \omega) = \chi_{mn}^{\mathrm{D}}(\mathbf{q}, \omega) - \chi_{mn}(\mathbf{q}), \qquad (A1)$$

with $\chi_{mn}^{\mathrm{D}}(\mathbf{q}, \omega) = \int (d\mathbf{k}/\Omega_{\mathrm{BZ}})\{(f_{n,\mathbf{k}} - f_{m,\mathbf{k}+\mathbf{q}})/[\varepsilon_{m,\mathbf{k}+\mathbf{q}} - \varepsilon_{n,\mathbf{k}} - \hbar(\omega + i\delta)]\}$ and $\chi_{mn}(\mathbf{q}, \omega) = \int (d\mathbf{k}/\Omega_{\mathrm{BZ}})[(f_{n,\mathbf{k}} - f_{m,\mathbf{k}+\mathbf{q}})/(\varepsilon_{m,\mathbf{k}+\mathbf{q}} - \varepsilon_{n,\mathbf{k}})]$. To facilitate comparisons, the resulting values are normalized by the adiabatic Lindhard term at zero momentum, $\mathrm{Re}\chi(q = 0, \omega = 0) = \chi_0$, contributed by the intraband transitions across the Fermi surface.

In MLG, we detected a significant modulation of the nonadiabatic $\chi^{\mathrm{NA}}(\mathbf{q}, \omega)$ by intraband transition of π^* [Fig. 5(a)]. Compared to the adiabatic $\mathrm{Re}\chi_{\pi^*\pi^*}(\mathbf{q})$ [gray curve in Fig. 5(b)], $\mathrm{Re}\chi_{\pi^*\pi^*}^{\mathrm{NA}}(\mathbf{q}, \omega)$ exhibits a positive peak

around 0.03 Å^{-1} [red curve in Fig. 5(b)]. This indicates that phonon hardening in MLG stems from the intraband nonadiabatic response. The $g_{\pi^*\pi^*}(\mathbf{q})$ of the LO phonon changes smoothly with momentum [Fig. 5(c)], thus not affecting the hardening results. In BLG, we detected two significant nonadiabatic modulations of $\chi^{\mathrm{NA}}(\mathbf{q}, \omega)$: $\chi_{\pi_1^*\pi_1^*}^{\mathrm{NA}}(\mathbf{q}, \omega)$ and $\chi_{\pi_1^*\pi_2^*}^{\mathrm{NA}}(\mathbf{q}, \omega)$ corresponding to π_1^* intraband and π_1^* to π_2^* interband transitions [Figs. 6(a), 6(b), and 6(d)], respectively. $\mathrm{Re}\chi_{\pi_1^*\pi_1^*}^{\mathrm{NA}}(\mathbf{q}, \omega)$ exhibits similar behaviors to the MLG, but the $\mathrm{Re}\chi_{\pi_1^*\pi_2^*}^{\mathrm{NA}}(\mathbf{q}, \omega)$ exhibits the opposite behaviors to the $\mathrm{Re}\chi_{\pi_1^*\pi_1^*}^{\mathrm{NA}}(\mathbf{q}, \omega)$. The tips of $\mathrm{Re}\chi_{\pi_1^*\pi_1^*}^{\mathrm{NA}}(\mathbf{q}, \omega)$ and $\mathrm{Re}\chi_{\pi_1^*\pi_2^*}^{\mathrm{NA}}(\mathbf{q}, \omega)$ are at almost the same momentum position, suggesting potential cancellation effects between them. Intriguingly, the magnitudes of the $g(\mathbf{q})$ for the S LO and AS LO modes in BLG vary significantly [Figs. 6(c) and 6(e)]. The EPCs of S LO and AS LO modes are predominantly governed by π_1^* intraband transition and π_1^* to π_2^* interband transition, respectively.

If we roughly use $|g_{mn}(\mathbf{q})|^2 \mathrm{Re}\chi_{mn}^{\mathrm{NA}}(\mathbf{q}, \omega)$ to estimate the magnitude of the phonon self-energies, we find that the self-energy of AS LO phonon near the point is negative, indicating softening. This is consistent with our observed results in BLG. For the S LO phonon, however, at small momentum (< 0.1 Å^{-1}), $g_{\pi_1^*\pi_1^*}(\mathbf{q})$ is significantly larger than $g_{\pi_1^*\pi_2^*}(\mathbf{q})$. This indicates that the phonon self-energy of S LO mode is dominated by intraband transitions, exhibiting similar hardening behaviors to the LO phonon in
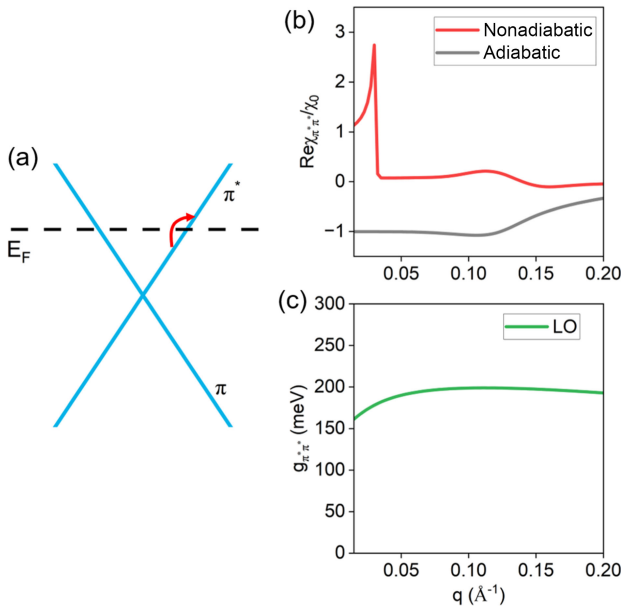

FIG. 5. Band-resolved nonadiabatic EPCs of MLG. (a) Schematic of the energy bands and band transitions. (b) The real parts of nonadiabatic (red curve) and adiabatic (gray curve) Lindhard functions for intraband transitions [red arrow in (a)]. (c) Electron-phonon matrix elements for LO mode associated with the intraband transitions.
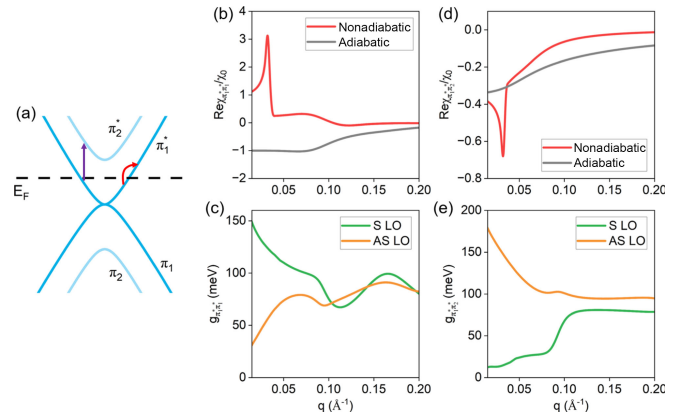

FIG. 6. Band-resolved nonadiabatic EPCs of BLG. (a) Schematic of the energy bands and band transitions. (b),(d) The real parts of nonadiabatic (red curve) and adiabatic (gray curve) Lindhard functions for intraband [red arrow in (a)] and interband [purple arrow in (a)] transitions, respectively. (c),(e) Electron-phonon matrix elements for S LO (green curves) and AS LO (orange curves) modes associated with the intraband and interband transitions, respectively.

MLG, which is consistent with our calculated results (Fig. S8 in SM [32]). The nonadiabatic analysis of the LO phonon in MLG and the S LO phonon in BLG reveals that the intraband contribution of dynamic Lindhard function is the primary cause of phonon hardening. This also indicates that the above analysis is applicable to general doped 2D materials, with phonon hardening being a universal phenomenon in doped 2D materials.